Chemical Science

ROYAL SOCIETY OF CHEMISTRY

EDGE ARTICLE

View Article Online
View Journal

Cite this: DOI: 10.1039/d6sc03302d

All publication charges for this article have been paid for by the Royal Society of Chemistry

Received 21st April 2026
Accepted 10th May 2026

DOI: 10.1039/d6sc03302d

rsc.li/chemical-science

Tetraphenylborate-based anionic metal–organic framework as an efficient single-ion conductor for solid-state sodium batteries

Xiaoxin Liu,†[a] Zhiwei Lu,†[a] Qianyi Zhao,*[a] Shujun Li,*[a] Jie Zhang,[a] Xuenian Chen[ab] and Qingchun Xia*[a]

Rechargeable sodium batteries (RSBs) have emerged as promising candidates in the post-lithium electrification era. However, their applications are often complicated by their inherent reactivity with flammable liquid electrolytes, which leads to dendrite growth, parasitic side reactions, and rapid performance degradation. In particular, conventional dual-ion electrolytes can exacerbate uncontrolled mossy and dendritic sodium metal growth, severely compromising their performance. In this work, we propose a tetraphenylborate-supported anionic metal–organic framework (MOF) as a promising single-ion conductive electrolyte to address the limitations of liquid dual-ion electrolytes. The anionic MOF is synthesized by reacting the sodium tetraphenylborate [$Na^+B(PhCOOH)_4^-$] building block with a Zr_6-oxo cluster. Na^+ counterions are directly encapsulated and serve as the free mobile charge carrier, achieving an ionic conductivity of 0.407 mS cm^{-1}, an activation energy of 0.19 eV, and a Na^+ transference number of 0.90. The developed anionic MOF-based solid-state electrolyte exhibits good interfacial compatibility with sodium metal and excellent rate performance. A combination of these properties enables the assembled solid-state RSB to deliver a remarkable capacity of 529 mA h g^{-1} at 0.1 A g^{-1} under ambient conditions and retain 424 mA h g^{-1} at 2 A g^{-1}, with a capacity retention of 93.8% after 2500 charge–discharge cycles. Moreover, the fabricated solid-state RSB can operate stably within a temperature range of −40 to 70 °C and at current densities from 0.1 to 10 A g^{-1}. Furthermore, Na^+ ions in the anionic MOF can be exchanged with K^+ and Zn^{2+}, establishing this anionic MOF as a versatile single-ion solid electrolyte for solid-state potassium and zinc batteries, which deliver the capacities of 437 and 554 mA h g^{-1}, respectively. This work not only establishes anionic MOFs as versatile and promising solid-state electrolytes for various types of solid-state batteries but also outlines a design blueprint for other anionic porous materials in energy storage.

Introduction

The escalating demand for sustainable energy, driven by the twin pressures of fossil fuel depletion and natural resource scarcity, has catalyzed intensive research into advanced energy storage systems that achieve both high energy density and safety performance.[1–3] Among the various candidates, rechargeable sodium batteries (RSBs) have emerged as promising candidates in the post-lithium electrification era,[4–6] owing to their high theoretical specific capacity (1165 mA h g^{-1}), low redox potential (−2.71 V *vs.* SHE), abundant natural reserves, and ready accessibility.[5,7–10] However, the implementation of sodium metal anodes is complicated by their inherent reactivity with flammable liquid electrolytes, which leads to dendrite growth, parasitic side reactions, and rapid performance degradation.[11,12] To overcome these limitations, extensive efforts have been devoted to interface engineering,[13–17] alloy anodes,[18–20] and solid-state electrolytes (SSEs).[21,22] Among these, SSEs have been proposed as a particularly promising avenue to address the safety concerns associated with organic liquid electrolytes, as they eliminate leakage risks and exhibit negligible flammability.[23–26]

Among various types of SSEs, metal–organic frameworks (MOFs) based SSEs have received significant attention by virtue of their designable and well-ordered porous structures.[27–31] These characteristics enable the incorporation of high-density charged species and offer additional space for hosting guest molecules as electrolytes within a confined volume.[32,33] Conventionally, most MOF-based solid electrolytes, which incorporate extrinsic metal salts into their frameworks,[34] are dual-ion conductors in which both metal ions (*e.g.*, Na^+) and

[a]*Henan Key Laboratory of Boron Chemistry and Advanced Materials, School of Chemistry and Chemical Engineering, Henan Normal University. Xinxiang, Henan 453007, China*

[b]*College of Chemistry, Zhengzhou University, Zhengzhou 450001, China. E-mail: qyzhao@htu.edu.cn; lisj@htu.edu.cn; xiaqingchun@htu.edu.cn*

† X. Liu and Z. Lu contributed equally to this work.

counter anions migrate between the anode and cathode during the alternating charge–discharge process.[35–37] However, the presence of mobile anions within the pore leads to a low transference number and undesirable polarization effects.[38,39] Such polarization causes an uneven electric field, which in turn results in uneven Na^+ fluxes within the frameworks.[40] This triggers nonuniform Na^+ plating/stripping on the anodic surface, leading to uncontrolled mossy and dendritic metal growth.[41] Such growth severely compromises rate performance, reduces coulombic efficiency, deteriorates capacity fading, and even causes short circuits. Therefore, the presence of redundant and undesirable mobile anions is undoubtedly the bottleneck that must be overcome to ensure a bright future for the RSBs.[27,42]

To date, the construction and application of anionic MOFs as single-ion conductive electrolytes has emerged as a promising strategy to facilitate uniform Na^+ flux and suppress dendrite formation. These frameworks feature periodic negative charge centers that provide continuous hopping sites for Na^+ to travel along the well-defined anionic channels, thereby achieving high ionic conductivity by simultaneously lowering the activation energy and significantly increasing the cation transference number. For the construction of anionic MOFs, the most straightforward strategy is to use ligands with inherent cation–anion structures,[43,44] such as sodium tetraphenylborate (Fig. 1a). The anionic tetraphenylborates form the framework and are permanently fixed within the pores, while the charge-balancing Na^+ ions are encapsulated in the anionic MOF and serve as the free mobile charge carriers to produce a single sodium-ion solid electrolyte. We previously showed that tetraphenylborate-based anionic MOFs can be employed as single-ion conductive electrolytes for lithium and zinc batteries.[44,45]

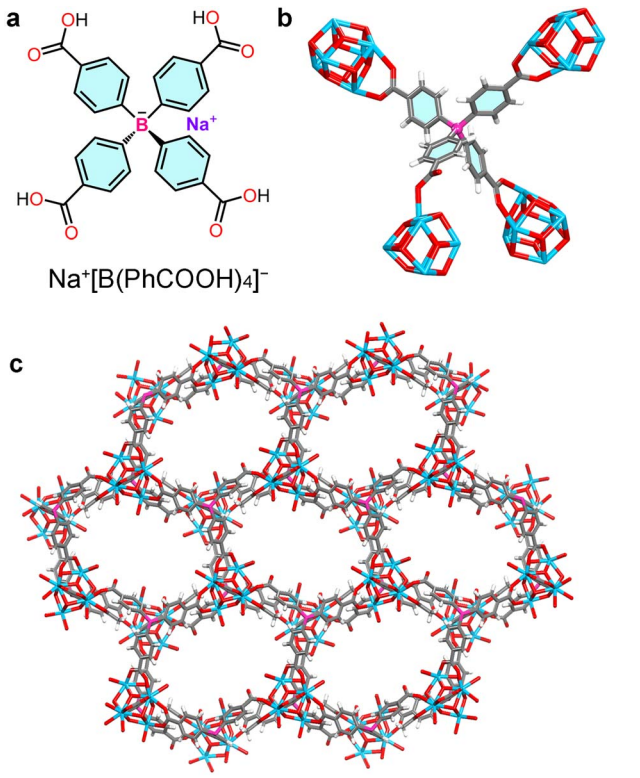

Fig. 1 (a) Molecular structure of the $Na^+[B(PhCOOH)_4]^-$ ligand. (b) The linker conformation in 2^{Na}. (c) 3D porous structure of 2^{Na}.

In this work, we continuously demonstrated that such anionic MOFs can function as a promising single-ion conductor for RSBs. We first successfully synthesized a robust Zr-based anionic framework from the carboxylic acid functionalized sodium tetraphenylborate $[Na^+B(PhCOOH)_4^-]$ ligand. Acting as a single-ion Na^+ conductor, the anionic MOF exhibited excellent ionic conductivity, impressive Na^+ transference number, low activation energy, wide electrochemical window, and superior rate performance. These advantageous characteristics remained stable across an extensive temperature range from −40 to 120 °C, with the ionic conductivity consistently satisfying the rigorous requirements for solid-state RSBs. Coupling the sodium metal as the anode and CityU-36 as the cathode,[8] the assembled solid-state RSB delivered a remarkable capacity of 529 mA h g^{-1} at 0.1 A g^{-1} under ambient conditions and retained 424 mA h g^{-1} when the current density was increased to 2 A g^{-1}, with a capacity retention of 93.8% after 2500 charge–discharge cycles. Moreover, the fabricated solid-state RSB can operate stably within a temperature range of −40 to 70 °C and at current densities from 0.1 to 10 A g^{-1}. Moreover, our single-ion Na^+ conductor also exhibited good compatibility with various cathodes, including PTCDA (3,4,9,10-perylenetetracarboxylic dianhydride), TiS_2, and MoS_2, enabling the corresponding RSBs to display good rate performance within the voltage of 1.5–3.5 V, 1.1–3.0 V, and 0.1–2.5 V, respectively. Last but not least, the exchangeability of Na^+ with both K^+ and Zn^{2+} empowers the anionic framework to serve as a versatile single-ion conducting electrolyte for both solid-state potassium and zinc battery systems, with all corresponding batteries displaying good rate performance. This work provides a promising and generalizable strategy for designing advanced solid-state electrolytes to facilitate the development of next-generation solid-state batteries.

Results and discussion

Anionic MOF 2^{Na} was synthesized through a solvothermal reaction between the anionic tetraphenylborate ligand $Na^+[B(PhCOOH)_4]^-$ and $ZrCl_4$ in a mixture of dimethylformamide (DMF) and acetic acid (HAc) at 100 °C for 12 hours. Colorless single crystals were isolated in ~63% yield, with the formula of $Na_2 \cdot \{Zr_6O_4(OH)_7(H_2O)(CH_3COO)[B(PhCOO)_4]_2\}$ as determined by structural analyses, including single crystal X-ray diffraction (SC-XRD), Fourier transform infrared spectroscopy (FT-IR), inductively coupled plasma mass spectrometry (ICP-MS), and thermogravimetric analysis (TGA).

SC-XRD analysis revealed that 2^{Na} crystallized in the orthorhombic space group *Pnma* with lattice parameters a = 25.1997(5) Å, b = 30.0943(4) Å, c = 17.3014(3) Å, and V = 13 120.8(4) $Å^3$. In 2^{Na}, the Zr_6 cluster is capped by nine carboxylate groups (Fig. S1), eight of which originate from eight different $B(PhCOO)_4^{5-}$ ligands, while the remaining one comes from the terminal acetic acid, thereby giving an unusual 8-connected Zr_6

cluster. For the $B(PhCOO)_4^{5-}$ ligand, its four carboxylate groups exhibit two coordination modes: three adopt a bidentate coordination mode, while the remaining one is monodentate (Fig. 1b). Each BPh_4^{5-} ligand is linked to four Zr_6 clusters, and each Zr_6 cluster is linked by eight BPh_4^{5-} ligands, forming an anionic network with the shortest B···B distance of ~9.20(5) Å. As shown in Fig. 1c and S3, this connectivity is unprecedented for zirconium MOFs. ToposPro analysis revealed the formation of the **ken** topology as registered in the RCSR database, in which the 8-connected Zr_6 clusters serve as bicapped trigonal prismatic building blocks bridged *via* the 4-connected T_d linkers to form a unique (4, 8)-connected network. This topology features a 1D elongated hexagonal channel with a cross-section of ~7.8 × 20.4 $Å^2$ running along the *b*-axis (Fig. 1c and S3). Six adjacent channels are then connected *via* 11.1 × 13.6 Å rhombic windows to create an interconnected 3D anionic framework that is charge-balanced by Na^+ cations (Fig. S5). Unfortunately, SC-XRD could not resolve the Na^+ cations within the framework, indicating that Na^+ ions are not confined but exhibit rather high freedom in the framework. This characteristic makes $\mathbf{2^{Na}}$ suitable as the single-ion solid electrolyte for sodium solid-state batteries. SEM-EDS mapping analysis of a single crystal indicated the presence of Na^+ ions with a uniform distribution throughout the crystal (Fig. S6). ICP-MS analysis of the digested sample provided the content of Na^+ to be 2.90 wt%.

PLATON calculations showed that $\mathbf{2^{Na}}$ has about 56.2% of the total volume for guest inclusion.[46] The phase purity was confirmed by the comparison of the experimental power X-ray diffraction (PXRD) pattern with that calculated from the single-crystal structure (Fig. 2a). Nitrogen sorption measurements on activated $\mathbf{2^{Na}}$ revealed a Type-I isotherm with a Brunauer–Emmett–Teller (BET) area of 583 $m^2\ g^{-1}$ (Fig. S7). Pore size distribution derived from the nonlocal density functional theory model (NLDFT) indicated the presence of regular ~16.2 Å pores (Fig. S8), thereby facilitating the rapid transport of Na^+ within the pore. Thermogravimetric analysis (TGA) revealed that guest molecules in the anionic framework could be readily removed, and the anionic framework started to decompose at about 470 °C (Fig. S10). Variable temperature PXRD (VT-XRD) indicated that the structure and crystallinity integrity could be preserved up to 300 °C in open air (Fig. 2a). Chemical stability was also evaluated by PXRD, N_2 sorption, and ^{11}B NMR analysis on $\mathbf{2^{Na}}$ after soaking in 1 M HCl (aq) and 1 M NaOH (aq) at room temperature for 24 h. The recovered samples exhibited little weight loss after being thoroughly washed and dried. PXRD patterns were almost the same as the original sample after chemical stability testing (Fig. 2a). N_2 adsorption measurements provided BET surface areas of 519 and 368 $m^2\ g^{-1}$, respectively, confirming the framework stability and permanent porosity (Fig. S7). After removal of the anionic framework, ^{11}B NMR analysis of these solutions showed no detectable B signal, indicating that neither stoichiometric nor substoichiometric amounts of decomposition occurred during these treatments. These recovered samples were then decomposed by 3 M NaOH, and the resulting ^{11}B NMR spectra were consistent with the $Na^+[B(PhCOOH)_4]^-$ ligand (Fig. S11), demonstrating the robustness of the C–B bond. The electrochemical stability was then evaluated by cyclic voltammetry (CV) and linear sweep voltammetry (LSV) measurements at room temperature. CV measurement displayed no significant current flow corresponding to electrolyte decomposition up to 3.5 V (Fig. S12). LSV measurement exhibited that the oxidation voltages of the anionic framework were 3.59, 3.68, 3.87, and 3.87 V *vs.* Na/Na^+ when Cu, stainless steel (SS), Mo, and Ti were used as current collectors, respectively (Fig. 2d). Both CV and LSV measurements revealed that this anionic framework can be employed as a solid-state electrolyte that adapts to most available cathodes of sodium batteries with high energy density.

We subsequently employed $\mathbf{2^{Na}}$ as a competitive single Na-ion solid-state conductor. Before the ionic conductivity measurement, $\mathbf{2^{Na}}$ was thoroughly washed with THF and then dried at 120 °C under vacuum to remove any residue in the pores. A trace amount of propylene carbonate (PC) solvent was necessary not only to solvate the inside free Na^+ ions but also to wet the anionic pores and the interfaces between MOF particles. This facilitates efficient Na^+ ion migration, which involves both intrinsic ion diffusion along anionic channels and extrinsic transport across interparticle phases. We soaked $\mathbf{2^{Na}}$ in PC solvent for 24 h, briefly washed with THF, and dried it under vacuum. The resulting powder was then mechanically pressed into a pellet and sandwiched between two stainless steel electrodes in an airtight cell. The Na^+ ion conductivity was assessed by alternating current (AC) impedance spectroscopy over a frequency range of 100 kHz to 1 Hz and temperatures from −40 °C to 120 °C. As shown in Fig. 2b, the resistance of $\mathbf{2^{Na}}$ decreases with increasing temperature and exhibits Arrhenius behavior. The ionic conductivity was calculated to be 0.407 mS cm^{-1} at 25 °C, increasing to 4.27 mS cm^{-1} at 120 °C and remaining at 0.11 mS cm^{-1} at −25 °C. The activation energy (E_a) was then acquired by fitting the temperature-dependent conductivity curves, and the value was estimated to be 0.19 eV (Fig. S14). Electronic conduction was then studied by direct current (DC) polarization measurement, yielding a value of 1.16 × 10^{-9} S cm^{-1} (Fig. 2c). This value is five orders of magnitude lower than the ionic conductivity, highlighting the significant electrical insulation of the anionic framework that prevents current flow through the electrolyte. The Na^+ ion transfer number (t_{Na^+}) was measured by using the Evans method, and the value was estimated to be as high as 0.90 (Fig. 2c). The transference number of electronic conductivity was also measured with a value less than 0.01%, thereby confirming that the observed conductivity arises from the single Na^+ ion migration within the anionic pores.

We further evaluated the compatibility of $\mathbf{2^{Na}}$ with the metallic Na anode. We first assembled a $Na/\mathbf{2^{Na}}/Cu$ half-cell to evaluate the coulombic efficiency of Na plating/stripping on Cu foil. Fig. S15 displays the coulombic efficiency of the half-cell at 1 mA cm^{-2} with a capacity of 1 mA h cm^{-2}. Notably, the half-cell demonstrated a stable cycle life of 240 cycles, with a coulombic efficiency of up to 99.7%. Moreover, during this plating/stripping experiment, the half-cell exhibited a stable voltage profile with a minimal voltage lag of 78 mV. Compatibility was also reflected by the nucleation overpotential (NOP), and this value was found to be 76 mV (Fig. S16), indicating a favorable

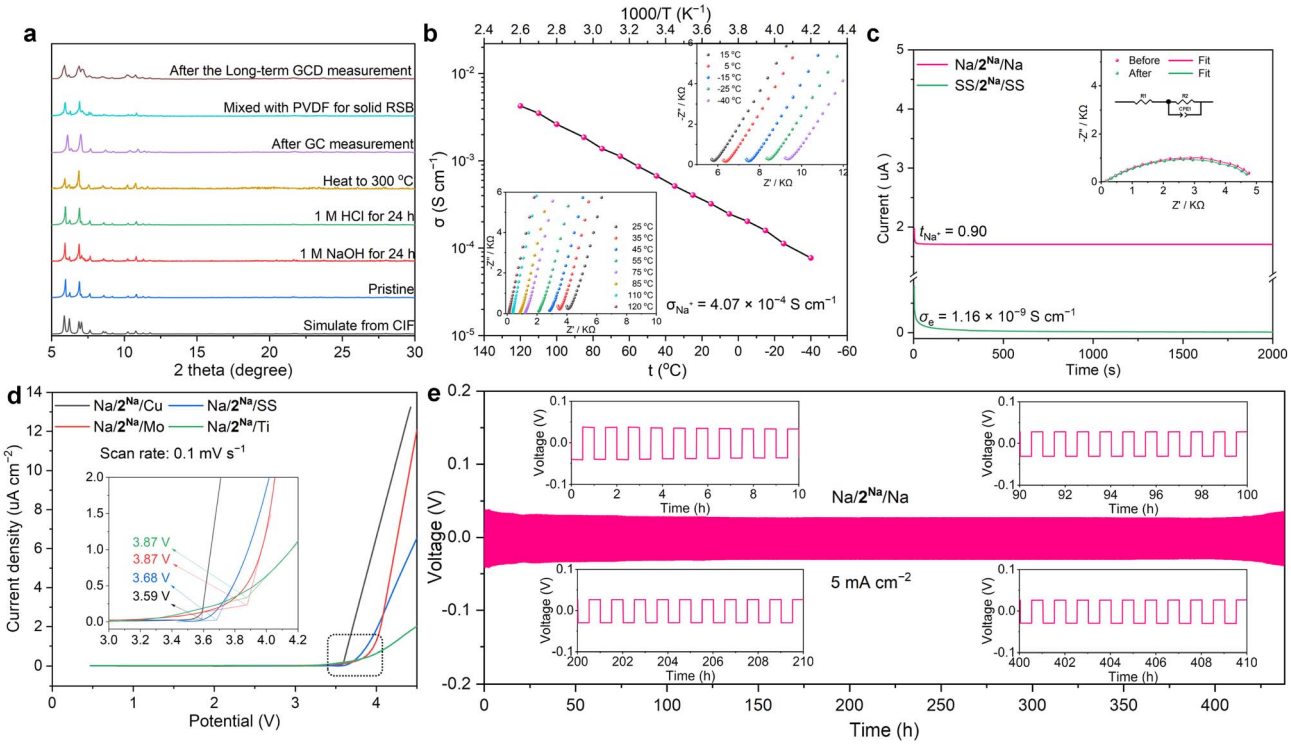

Fig. 2 (a) PXRD patterns of $\mathbf{2}^{\mathbf{Na}}$ after various treatments. (b) Ionic conductivity of $\mathbf{2}^{\mathbf{Na}}$ as a function of temperature in the range from −40 to 120 °C. Inset: Nyquist plots for $\mathbf{2}^{\mathbf{Na}}$. (c) CA curves of the Na/$\mathbf{2}^{\mathbf{Na}}$/Na and SS/$\mathbf{2}^{\mathbf{Na}}$/SS cells at a polarized voltage of 10 mV. Inset: Nyquist plots obtained before and after polarization. (d) LSV measurements for the asymmetric cells at room temperature at a scan speed of 0.1 mV s^{-1}. (e) GC performance of the Na/$\mathbf{2}^{\mathbf{Na}}$/Na symmetrical cell at a current density of 5 mA cm^{-2} at room temperature.

interfacial compatibility between $\mathbf{2}^{\mathbf{Na}}$ and the metallic sodium anode.

Subsequently, we assembled a symmetric Na/$\mathbf{2}^{\mathbf{Na}}$/Na cell to evaluate its electrochemical performance and the long-term cycling stability between the sodium metal anode and $\mathbf{2}^{\mathbf{Na}}$ electrolyte. CV measurement revealed that the initial deposition potential of Na^+ was only 68 mV (Fig. S17). Chronoamperometry (CA) measurement highlighted that the current density exhibited a rapid increase during the initial 16 seconds and subsequently stabilized in the following plating process (Fig. S18). Both CV and CA measurements demonstrate a uniform nucleation/deposition process without Na dendrite formation on the surface of the sodium electrode. The interfacial characteristic of this symmetric cell was further analyzed by using Tafel measurement. The Tafel curve, extrapolated from the linear polarization region, yielded a high exchange current density (j_0) of 43 mA cm^{-2} (Fig. S19), indicating a stable interface for the rapid sodium transfer in this symmetric cell. Moreover, this stability further highlighted that the combination of the robust framework, well-distributed negative charges, and single-ion transport characteristics collectively enables uniform Na^+ transport and deposition.

Galvanostatic cycling (GC) measurement was then conducted to assess the rate capability and cycling stability. The rate performance was evaluated at a current density of 5 mA cm^{-2} with a fixed areal capacity of 2.5 mA h cm^{-2} at room temperature. As shown in Fig. 2e, the symmetric Na/$\mathbf{2}^{\mathbf{Na}}$/Na cell exhibited a relatively low overpotential of 28 mV for over 400 hours without significant fluctuations in polarization potential. The enlarged voltage profile showed a flat voltage plateau in the whole charge–discharge cycles, reflecting a uniform Na-ion flux directed by the anionic framework $\mathbf{2}^{\mathbf{Na}}$ electrolyte. Building on these promising results, we further investigated the rate performance by fixing the deposition capacity at 1 mA h cm^{-2} and varying the current density from 5 to 30 mA cm^{-2}. As shown in Fig. S20, the symmetric cell exhibited excellent stability and maintained a voltage of around 650 mV even at a high current density of 30 mA cm^{-2} without short-circuiting. Furthermore, the symmetric cell also demonstrated excellent reversibility, with the voltage returning to its original level immediately upon switching the current density back to 5 mA cm^{-2}.

The calendar ageing of the symmetric cell was assessed by tracking its resistance, showing a nearly constant total resistance (~14.5 Ω) throughout the process (Fig. S21). The recovered $\mathbf{2}^{\mathbf{Na}}$ electrolyte still retained its crystallinity, as confirmed by PXRD (Fig. 2a). Its porous structure and Na^+ content remained almost unchanged according to the N_2 sorption and ICP-MS analysis, respectively. In addition, SEM images of the cycled sodium metal electrode exhibited a clean and flat surface (Fig. S22), visually demonstrating that single Na^+ ion migration within the anionic framework can circumvent polarization effects and suppress the formation of sodium dendrites.

The electrochemical performance of $\mathbf{2}^{\mathbf{Na}}$ as the single sodium-ion solid electrolyte was studied using a standard coin-

type cell with sodium foil as the anode and CityU-36 as the cathode (Fig. S23).[8] Fig. S24 shows the first five CV curves of the solid-state RSB at 1.6 mV s^{-1} in 0.1–3.0 V (*vs.* Na^+/Na). Three pairs of reduction/oxidation peaks are observed at 0.53/0.75 V, 0.66/0.94 V, and 0.93/1.12 V, indicating a reversible Na^+ insertion/extraction process. CV measurements at various scan rates were then conducted to investigate the kinetics of the Na^+ transport and insertion/extraction processes. As demonstrated in Fig. 3h, all CV curves exhibit a similar shape, and the peaks shift to higher polarization with the scan rate increasing from 0.2 to 1.6 mV s^{-1}, implying rate-dependent charge storage behavior in the fabricated solid-state RSB. The peak current (i) at various scan rates follows a power–law relationship with the scan rate (v): $i = av^b$, where a and b are fitting parameters. Generally, $b = 0.5$ represents the ion-intercalation process, and $b = 1$ indicates the capacitance-controlled behavior. Based on the corresponding log–log plot of i *vs.* v fitting results, the calculated b values for peaks 1, 2, 3, and 4 are 0.93, 0.71, 0.97, and 0.94 (Fig. 3i), respectively, indicating the pseudocapacitive reactions and fast Na^+ ion diffusion in the fabricated solid-state RSB. Deconvolution using the Dunn method further quantified that the total stored charge contributed by the surface redox reactions increases from 82.2% to over 99% as the scan rate increases from 0.2 to 1.6 mV s^{-1} (Fig. 3j and S25). This increase indicates a rapid pseudocapacitive process for Na^+ storage in this single-ion battery system. Furthermore, the diffusion coefficient of Na^+ (D_{Na}) in the solid-state RSB was determined *via* the galvanostatic intermittent titration technique (GITT). As shown in Fig. 3k, the calculated D_{Na} value mainly remains in the range of 10^{-10} to 10^{-12} cm^2 s^{-1} over the whole charge/discharge process. The high ion diffusion coefficient, combined with the low activation energy (0.24 eV) derived from temperature-dependent electrochemical measurements (Fig. S26 and S27), evidences the super Na^+ ion transport in the single-ion electrolyte $\mathbf{2^{Na}}$ and fast Na^+ insertion/extraction processes in our solid-state RSB.

Subsequently, the rate performance was evaluated *via* a galvanostatic charge–discharge (GCD) test. As shown in Fig. 3d, the GCD curves of the fabricated solid-state RSB revealed three distinct discharge plateaus at 1.00, 0.70, and 0.61 V, along with three corresponding charge plateaus at 0.82, 0.90, and 1.50 V, which aligned well with the features observed in the CV curves. The GCD performance was further assessed within a voltage range of 0.1–3.0 V at room temperature. As shown in Fig. 3c, the solid-state RSB delivered a high reversible capacity of 529 mA h g^{-1} at 0.1 A g^{-1}, and retained the capacities of 482, 468, 421, and 380 mA h g^{-1} at current densities of 0.3, 0.5, 1, and 3 A g^{-1}, respectively. Even when the current density was increased to 10 A g^{-1}, the battery still exhibited a reversible capacity of 47 mA h g^{-1}, and rapidly recovered to 522 mA h g^{-1} with the current density switching back to 0.1 A g^{-1}. The rate capability was also evaluated across a temperature range from −20 to 70 °C, as presented in Fig. 3e, f, and S28. At 70 °C, the battery delivered capacities of 611, 563, 532, and 433 mA h g^{-1} at current densities of 0.1, 0.5, 1, and 5 A g^{-1}, respectively. At −20 °C, it still provided capacities of 242, 147, 107 and 29 mA h g^{-1} at the same current densities. Even though the temperature dropped to −40 °C, the battery could still deliver a capacity of 185 mA h g^{-1} and rapidly recovered back to 522 mA h g^{-1} when the temperature returned to 30 °C (Fig. S29). We further evaluated the long-term GCD performance of the solid-state RSB. At a current density of 2 A g^{-1} (Fig. 3g), the solid-state RSB delivered an initial capacity of 424 mA h g^{-1}. This value gradually decreased to 402 mA h g^{-1} over the initial 25 cycles, then remained nearly unchanged in the following 2475 cycles, with a coulombic efficiency of near 100%, confirming the excellent reversibility of the solid-state RSB. Moreover, when the current density was further recorded at 1, 3, 5, and 8 A g^{-1}, the cell also delivered stable performance, retaining 100%, 85%, 73%, and 51% of its initial capacity after more than 2500 cycles with coulombic efficiencies remaining nearly unchanged throughout the entire cycling process (Fig. S31).

The self-discharge characteristic of the solid-state RSB was then evaluated after charging to 3.0 V. Following a 24-hour rest period at room temperature, the battery could maintain a stable voltage of 2.26 V and delivered a discharge capacity of 481 mA h g^{-1} with a 91% capacity retention (Fig. S32). Owing to this robust performance, our solid-state RSB was capable of powering brilliant red light-emitting diodes (Fig. S33). Upon disassembling the long-cycled battery, we observed that the sodium anode remained as smooth and bright as before (Fig. S34), and the single-ion solid electrolyte $\mathbf{2^{Na}}$ retained its structural integrity without any detectable cracks or voids (Fig. 2g). Our single-ion solid electrolyte could also tolerate other cathode materials, such as PTCDA (Fig. S35–S38), TiS_2 (Fig. S39–S42), and MoS_2 (Fig. S43–S46), enabling the formation of stable solid-state RSBs that achieved capacities of 114, 163, and 212 mA h g^{-1} with the voltage output range 1.5–3.5 V, 1.1–3.0 V, and 0.1–2.5 V, respectively. These three solid-state RSBs were also capable of undergoing more than 1000 consecutive charge/discharge cycles at room temperature. Therefore, we concluded that our anionic MOF electrode $\mathbf{2^{Na}}$ not only facilitated efficient Na^+ ion transport in its anionic channels but also exhibited excellent interfacial compatibility with metallic Na anode and cathode materials, including CitU-36 COF, PTCDA, TiS_2 and MoS_2, enabling effective utilization of Na metal and stable rate performance during the continuous plating/stripping and charge/discharge cycles.

Given the presence of free Na^+ ions and the readily accessible ion-exchange channels in $\mathbf{2^{Na}}$, we performed ion-exchange experiments with K^+ and Zn^{2+} to access single-ion conductors for rechargeable solid-state potassium (RPB) and zinc (RZB) batteries, respectively. Typically, the ion-exchange experiments were performed by immersing $\mathbf{2^{Na}}$ in a PC-saturated KI solution or a 2.0 M aqueous $Zn(NO_3)_2 \cdot 6H_2O$ solution at 80 °C, with the solution refreshed every 4 h for a total of five cycles. After the ion exchange completion, the precipitates were filtered, thoroughly washed with PC or water, and dried at 120 °C under vacuum to afford $\mathbf{2^K}$ and $\mathbf{2^{Zn}}$, respectively. PXRD patterns confirmed that $\mathbf{2^K}$ and $\mathbf{2^{Zn}}$ retained structural similarity to their pristine counterpart $\mathbf{2^{Na}}$ (Fig. 4b). N_2 adsorption experiments provided the BET surface areas of 416 and 311 m^2 g^{-1} for $\mathbf{2^K}$ and $\mathbf{2^{Zn}}$, respectively (Fig. S48). SEM-EDS mapping analysis of a single crystal at the microstructural level revealed a uniform distribution of the

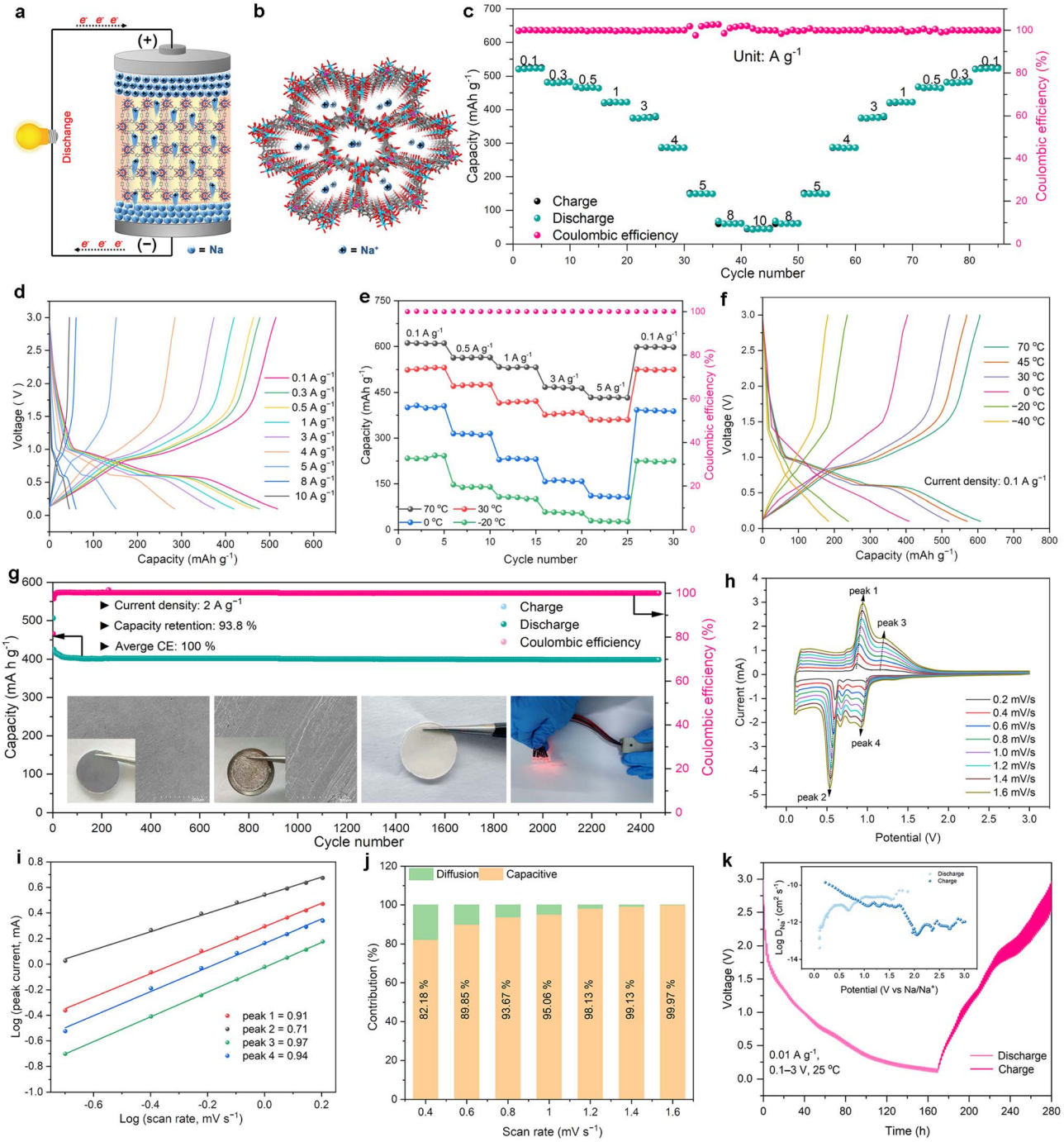

Fig. 3 (a) Schematic illustration of the solid-state RSB by using $\mathbf{2}^{Na}$ as the single-ion SSE. (b) Schematic illustration of the single Na^+ ion transportation in $\mathbf{2}^{Na}$. (c and d) Rate and cycling performance at current densities from 0.1 to 10 A g^{-1} at room temperature. (e) Rate and cycling performance at current densities from 0.1 to 5 A g^{-1} at 70, 30, 0, and −20 °C, respectively. (f) Capacity of the sodium battery at 70, 45, 30, 0, −20, and −40 °C at a current density of 0.1 A g^{-1}. (g) Long-term GCD performance of the battery at 2 A g^{-1}; insets: photographs and SEM morphologies of the sodium metal surface before and after cycling; the photograph of $\mathbf{2}^{Na}$ electrolyte; the fabricated solid-state RSB for lighting LED lamps. (h) CV curves of the solid-state RSB at various scan rates. (i) The relationship between peak current and scan rate. (j) Capacitive contributions in the fabricated solid-state RSB at various scan rates. (k) GITT curves and corresponding Na^+ diffusion coefficients in the fabricated solid-state RSB.

metal elements throughout the whole crystal (Fig. S49 and S50). EIS measurements indicated the room-temperature conductivities of 0.34 and 0.32 mS cm^{-1} for $\mathbf{2}^{K}$ and $\mathbf{2}^{Zn}$ (Fig. 4c, S51, and S56). The activation energies within the temperature range from −40 to 120 °C were determined to be 0.20 and 0.19 eV (Fig. S52 and S57). The average ion transference numbers were calculated to be 0.87 and 0.80 (Fig. S53 and S58). We then assembled solid-state RPBs and RZBs using $\mathbf{2}^{K}$ and $\mathbf{2}^{Zn}$ as the respective

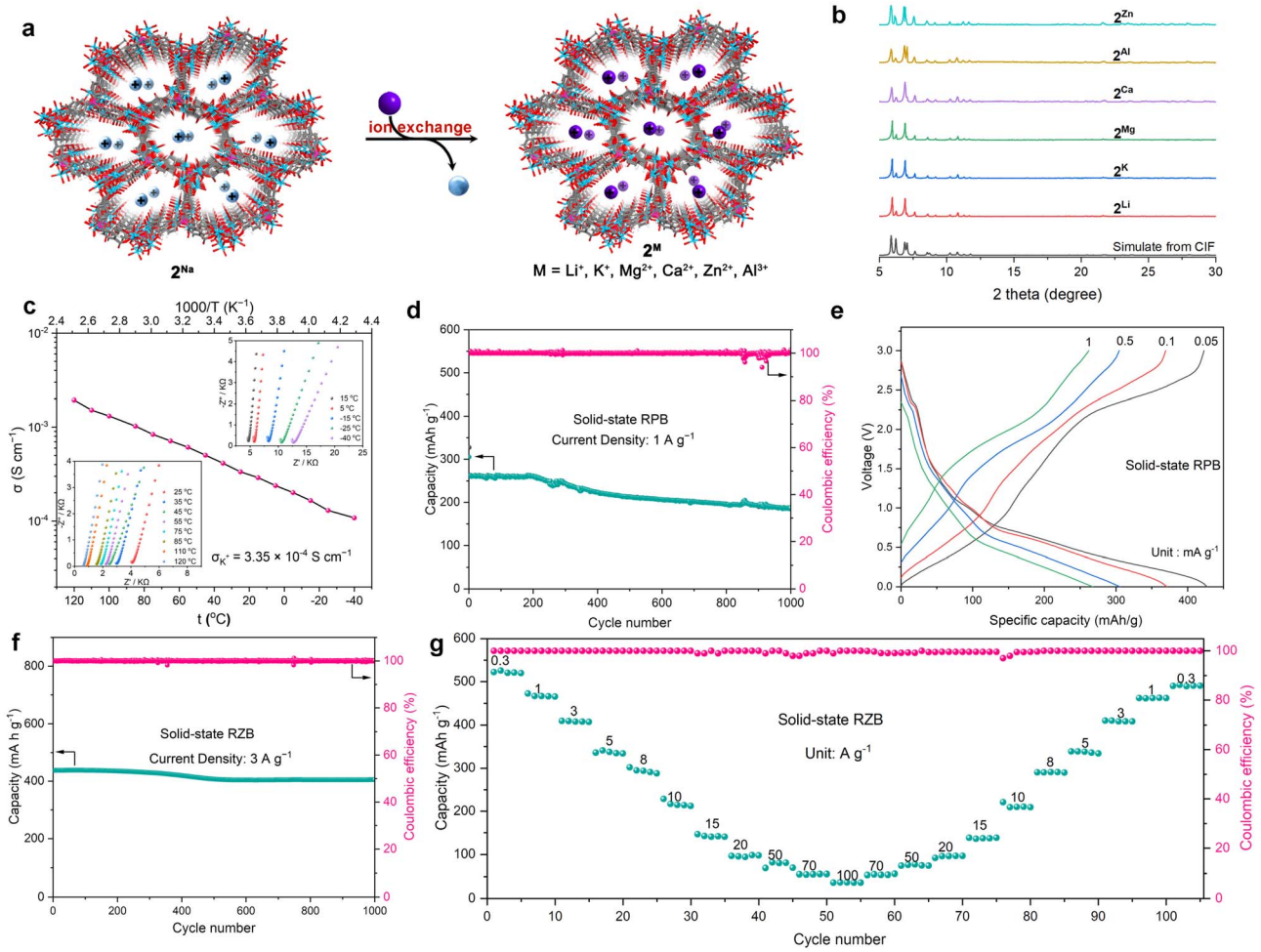

Fig. 4 (a) Schematic illustration of tetraphenylborate-based anionic MOFs as a versatile single-ion conductor through ion-exchange. (b) PXRD patterns of 2^{M}, M = Li, K, Mg, Ca, Zn, and Al. (c) Ionic conductivity of 2^{K} as a function of temperature in the range from −40 to 120 °C. Inset: Nyquist plots for 2^{K}. (d) Long-term GCD performance of the RPB at 1 A g^{-1}. (e) Rate performance of the RPB at current densities from 0.05 to 1 A g^{-1} at room temperature. (f) Long-term GCD performance of the RZB at 3 A g^{-1}. (g) Rate and cycling performance of the RZB at current densities from 0.3 to 100 A g^{-1} at room temperature.

electrolytes to evaluate the general applicability of the anionic framework. Specifically, the TQBQ-COF was used as the cathode coupled with 2^{K} and potassium foil for the solid-state RPB,[2,47] while for the solid-state RZB, our previously reported $NH_4V_4O_{10}$ (NVO) served as the cathode paired with 2^{Zn} and zinc foil.[45] As shown in Fig. 4e, the fabricated solid-state RPB could deliver a high reversible capacity of 439 mA h g^{-1} at 0.05 A g^{-1}, and retained a capacity of 261 mA h g^{-1} at 1 A g^{-1}, with the voltage output range of 0–3 V. Long-term GCD testing at a current density of 1 A g^{-1} further revealed outstanding stability of the anionic framework, with a high specific capacity of 187 mA h g^{-1} retained after 1000 cycles. Fig. 4g displays the GCD curve of the RZB, which delivered discharge capacities of 524, 465, 338, and 222 mA h g^{-1} at current densities of 0.3, 1.0, 5.0, and 10 A g^{-1}. Notably, even at an ultrahigh rate of 100 A g^{-1}, our RZB still delivered a capacity of 38 mA h g^{-1} and rapidly recovered to 522 mA h g^{-1} when the current density was switched back to 0.3 A g^{-1}. The long-term GCD stability was also evaluated at a current density of 3 A g^{-1}. As shown in Fig. 4f, the fabricated RZB exhibited an initial discharge capacity of 437 mA h g^{-1} and retained a specific capacity of 405 mA h g^{-1} after 1000 cycles. Consequently, our anionic MOF can be employed as a versatile solid electrolyte, making it suitable for various types of solid-state batteries.

Conclusions

In conclusion, we have presented an anionic MOF (2^{Na}) based on the tetraphenylborate building block, $Na^{+}[B(PhCOOH)_4]^{-}$ as a viable single-ion electrolyte for sodium batteries. In this structure, Na^{+} counterions are directly encapsulated and serve as the free mobile charge carriers, achieving an ionic conductivity of 4.07×10^{-4} S cm^{-1}, a low activation energy of 0.19 eV, and a high Na^{+} transference number of 0.90. Acting as a single-ion solid-state electrolyte, the obtained 2^{Na} exhibits good interfacial compatibility with sodium metal and excellent rate performance. Its well-defined porous architecture, coupled with a homogeneous distribution of BPh_4^{-} anionic centers, provides

an efficient pathway for rapid Na^+ conduction and deposition. These combined properties enable the assembled solid-state sodium battery to deliver high performance, including superior rate capability and long-term cycling stability. This promising performance underscores its significant potential for commercial applications. Moreover, the Na^+ ions in the anionic metal–organic framework can be exchanged with K^+ and Zn^{2+}, thereby establishing this tetraphenylborate-supported anionic MOF as a versatile platform for single-ion solid electrolytes in various battery systems. This work not only highlights the advantages of the anionic framework as a single-ion solid-state electrolyte in solid-state RSBs, RPBs, and RZBs, but also suggests its potential applicability in other systems, including solid-state magnesium and calcium batteries.

Author contributions

Q. Xia conceived and designed the experiments. X. Liu and Z. Lu performed the experiments and analyzed the data. Q. Xia and X. Liu carried out single crystal X-ray analyses. X. Liu and Q. Zhao performed the full cell measurements. J. Zhang and X. Chen provided useful discussions and insights. Q. Xia, Q. Zhao, and S. Li wrote the paper. All authors contributed to this manuscript.

Conflicts of interest

The authors declare no competing interests.

Data availability

All the supporting data associated with this work are available in the supplementary information (SI).

CCDC 2542313 contains the supplementary crystallographic data for this paper.[48]

Supplementary information is available. See DOI: https://doi.org/10.1039/d6sc03302d.

Acknowledgements

This work was financially supported by the Natural Science Foundation of China (Grant No. 22471062 and 22571070) and the Natural Science Foundation of Henan Province (252300421042).

Notes and references

1 J. Pan, Z. Sun, X. Wu, T. Liu, Y. Xing, J. Chen, Z. Xue, D. Tang, X. Dong, H. Zhang, H. Liu, Q. Wei, D.-L. Peng, K. Amine and Q. Zhang, *J. Am. Chem. Soc.*, 2025, **147**, 3047–3061.
2 R. Shi, L. Liu, Y. Lu, C. Wang, Y. Li, L. Li, Z. Yan and J. Chen, *Nat. Commun.*, 2020, **11**, 178.
3 X. Wang, Q. Fan, W. Wang, X. Liang, Z. Liu, L. Wang, Q. Kong, X. Li, C. C. Li, S. Wang, Z. Xue, Y. Ren, X. C. Zeng and Q. Liu, *Nat. Energy*, 2026, DOI: 10.1038/s41560-026-01995-x.
4 J. Chu, Z. Liu, J. Yu, H.-G. Wang, F. Cui and G. Zhu, *Nat. Commun.*, 2025, **16**, 3549.
5 Y. Guo, L. Cheng, X. Zhang, M. Qi, Y. Wei, S. Han, X. Su, H. G. Wang and L. Chen, *Angew. Chem., Int. Ed.*, 2025, **64**, e202510604.
6 W. Zuo, Z. Liu, A. Dopilka, Z. Yang, Y. Li, J. Kubal, H. Kim, F. Liu, P. Liu, A. T. Ngo, J. Nelson Weker, Z. Chen, R. Kostecki, J. Wulf-Knoerzer, V. Srinivasan, Y. Cui, K. Amine and G.-L. Xu, *Nat. Rev. Mater.*, 2026, **11**, 117–135.
7 X. Huang, H. Sun, X. Li, W. Zhu, L. Chen, T. Ma, S. Ding, T. Ma, Y. Dong, K. Zhang, F. Cheng, Q. Wei, L. Gao, J. Zhao, W. Zhang and J. Chen, *J. Am. Chem. Soc.*, 2024, **146**, 29391–29401.
8 F. Kang, L. Yan, Y. Cao, Z. Chen, Y. Zhao, X. Wang, Y. Zhang, L. Cheng, Q. Gu, J. Yang, F.-R. Chen, C.-S. Lee, Y. Wang and Q. Zhang, *J. Am. Chem. Soc.*, 2025, **147**, 26069–26078.
9 F. Kang, L. Yan, Z. Chen, Y. Zhang, Q. Gu, J. Yang, S. Xu, X. Wang, C. S. Lee, Y. Wang and Q. Zhang, *Angew. Chem., Int. Ed.*, 2024, **64**, e202417779.
10 T. Chen, J. Wang, B. Tan, K. J. Zhang, H. Banda, Y. Zhang, D.-H. Kim and M. Dincă, *J. Am. Chem. Soc.*, 2025, **147**, 6181–6192.
11 S. W. Ke, W. Li, L. Gao, J. Su, R. Luo, S. Yuan, P. He and J. L. Zuo, *Angew. Chem., Int. Ed.*, 2024, **64**, e202417493.
12 L. Liu, Y. Gong, Y. Tong, H. Tian, X. Wang, Y. Hu, S. Huang, W. Huang, S. Sharma, J. Cui, Y. Jin, W. Gong and W. Zhang, *CCS Chem.*, 2024, **6**, 1255–1263.
13 Y. Dong, C. Xu, H. Zhao, L. Chen, W. Shi, J. Irvine and Y. Lei, *Adv. Energy Mater.*, 2025, **16**, 2500407.
14 F. Ling, Z. Wu, J. Feng, Z. Wang, Z. Li, R. Bai, W. Du, H. Huo, X. Rui, H. Pan, Y. Yao and Y. Yu, *Adv. Mater.*, 2026, **38**, e21368.
15 S. Lou, F. Zhang, C. Fu, M. Chen, Y. Ma, G. Yin and J. Wang, *Adv. Mater.*, 2020, **33**, 2000721.
16 Y. Wu, H. Zhu, B. Wang, Z. Hou, Q. Ma, Q. Rong, Y. Chen, L. Chen, L. Zhou and W. Wei, *ACS Energy Lett.*, 2025, **10**, 2487–2497.
17 Y. Li, Q. Zhou, S. Weng, F. Ding, X. Qi, J. Lu, Y. Li, X. Zhang, X. Rong, Y. Lu, X. Wang, R. Xiao, H. Li, X. Huang, L. Chen and Y.-S. Hu, *Nat. Energy*, 2022, **7**, 511–519.
18 M. Peng, K. Shin, L. Jiang, Y. Jin, K. Zeng, X. Zhou and Y. Tang, *Angew. Chem., Int. Ed.*, 2022, **61**, e202206770.
19 X. Yu, S. Chen, B. Tang, X.-L. Li, J. Zhou, Y. Ren, J. Wei, C. Yang, Y. Guo, Z. Zhou and S.-H. Bo, *ACS Energy Lett.*, 2024, **9**, 4441–4449.
20 Z. Chen, Y. Li, L. Wang, J. Zhang, R. Dang, H. Yu, B. Wang, C. Xu, H. Li, Y. Li, Y. Li, L. Zhou, F. Xie, R. Xiao, Y. Lu, H. Li, X. Huang, L. Chen and Y.-S. Hu, *Nat. Energy*, 2026, **11**, 449–459.
21 X. Lin, S. Zhang, M. Yang, B. Xiao, Y. Zhao, J. Luo, J. Fu, C. Wang, X. Li, W. Li, F. Yang, H. Duan, J. Liang, B. Fu, H. Abdolvand, J. Guo, G. King and X. Sun, *Nat. Mater.*, 2024, **24**, 83–91.
22 Y. Yang, S. Yang, X. Xue, X. Zhang, Q. Li, Y. Yao, X. Rui, H. Pan and Y. Yu, *Adv. Mater.*, 2023, **36**, 2308332.
23 F. Makhlooghiazad, L. Miguel Guerrero Mejía, G. Rollo-Walker, D. Kourati, M. Galceran, F. Chen, M. Deschamps,

P. Howlett, L. A. O'Dell and M. Forsyth, *J. Am. Chem. Soc.*, 2024, **146**, 1992–2004.
24 X. Zhang, W. Li, Z. Wang, G. Shao and W. Chen, *Acc. Chem. Res.*, 2025, **58**, 3123–3136.
25 X. Wang, C. Zhang, M. Sawczyk, J. Sun, Q. Yuan, F. Chen, T. C. Mendes, P. C. Howlett, C. Fu, Y. Wang, X. Tan, D. J. Searles, P. Král, C. J. Hawker, A. K. Whittaker and M. Forsyth, *Nat. Mater.*, 2022, **21**, 1057–1065.
26 Q. Zhao, S. Stalin, C.-Z. Zhao and L. A. Archer, *Nat. Rev. Mater.*, 2020, **5**, 229–252.
27 T. Hou, W. Xu, X. Pei, L. Jiang, O. M. Yaghi and K. A. Persson, *J. Am. Chem. Soc.*, 2022, **144**, 13446–13450.
28 Y. Ouyang, W. Gong, Q. Zhang, J. Wang, S. Guo, Y. Xiao, D. Li, C. Wang, X. Sun, C. Wang and S. Huang, *Adv. Mater.*, 2023, **35**, 2304685.
29 W. Xue, C. D. Sewell, Q. Zhou and Z. Lin, *Angew. Chem., Int. Ed.*, 2022, **61**, e202206512.
30 R. Zhao, Y. Wu, Z. Liang, L. Gao, W. Xia, Y. Zhao and R. Zou, *Energy Environ. Sci.*, 2020, **13**, 2386–2403.
31 A. Iliescu, J. L. Andrews, J. J. Oppenheim and M. Dincă, *J. Am. Chem. Soc.*, 2023, **145**, 25962–25965.
32 S. Jiang, T. Lv, Y. Peng and H. Pang, *Adv. Sci.*, 2023, **10**, 2206887.
33 P. Dong, X. Zhang, W. Hiscox, J. Liu, J. Zamora, X. Li, M. Su, Q. Zhang, X. Guo, J. McCloy and M. K. Song, *Adv. Mater.*, 2023, **35**, 2211841.
34 Y. Yoshida, K. Kato and M. Sadakiyo, *J. Phys. Chem. C*, 2021, **125**, 21124–21130.
35 X. Wang, S. Jin and Z. Liu, *Chem. Commun.*, 2024, **60**, 5369–5390.
36 X. X. Wang, X. W. Chi, M. L. Li, D. H. Guan, C. L. Miao and J. J. Xu, *Adv. Funct. Mater.*, 2022, **32**, 2113235.
37 Y. Yoshida, T. Yamada, Y. Jing, T. Toyao, K.-i. Shimizu and M. Sadakiyo, *J. Am. Chem. Soc.*, 2022, **144**, 8669–8675.
38 L. Xu, X. Xiao, H. Tu, F. Zhu, J. Wang, H. Liu, W. Huang, W. Deng, H. Hou, T. Liu, X. Ji, K. Amine and G. Zou, *Adv. Mater.*, 2023, **35**, 2303193.
39 H. Bao, D. Chen, B. Liao, Y. Yi, R. Liu and Y. Sun, *Energy Fuels*, 2024, **38**, 11275–11283.
40 R. Zettl, S. Lunghammer, B. Gadermaier, A. Boulaoued, P. Johansson, H. M. R. Wilkening and I. Hanzu, *Adv. Energy Mater.*, 2021, **11**, 2003542.
41 H. Yang, B. Liu, J. Bright, S. Kasani, J. Yang, X. Zhang and N. Wu, *ACS Appl. Energy Mater.*, 2020, **3**, 4007–4013.
42 S. Park, I. Kristanto, G. Y. Jung, D. B. Ahn, K. Jeong, S. K. Kwak and S.-Y. Lee, *Chem. Sci.*, 2020, **11**, 11692–11698.
43 W. Xu, X. Pei, C. S. Diercks, H. Lyu, Z. Ji and O. M. Yaghi, *J. Am. Chem. Soc.*, 2019, **141**, 17522–17526.
44 Q. Xia, K. Han, X. Ma, P. Qiu, Z. Li and X. Chen, *Chem. Sci.*, 2024, **15**, 17579–17589.
45 Q. Xia, X. Ma, P. Qiu, G. Yuan and X. Chen, *J. Am. Chem. Soc.*, 2025, **147**, 23331–23338.
46 A. Spek, *J. Appl. Cryst.*, 2003, **36**, 7–13.
47 X.-L. Chen, M. Xie, Z.-L. Zheng, X. Luo, H. Jin, Y.-F. Chen, G.-Z. Yang, D.-S. Bin and D. Li, *J. Am. Chem. Soc.*, 2023, **145**, 5105–5113.
48 CCDC 2542313: Experimental Crystal Structure Determination, 2026, DOI: 10.5517/ccdc.csd.cc2rbh3q.